Shock interaction with three-dimensional face centered cubic array of particles

Y. Mehta, C. Neal, T. L. Jackson,* S. Balachandar, and S. Thakur
Department of Mechanical and Aerospace Engineering, University of Florida, Gainesville, Florida 32611, USA
(Received 3 June 2016; published 30 September 2016)

In this paper we present three-dimensional fully resolved numerical simulations of shock propagation in air over a face centered cubic (fcc) array of particles. It is well know that shock interaction with a single particle results in nonmonotonic drag on the particle and that the peak force is an order of magnitude greater than the steady-state force. However, there is currently a substantial lack of numerical results for shock propagation over multiple particles. We therefore compute the unsteady inviscid drag coefficient as a function of time for the fcc array of particles and investigate the effect of varying the shock Mach number and the volume fraction. We compare the unsteady drag for the fcc array against the unsteady drag for a single spherical particle and against the unsteady drag for a structured one-dimensional array of spherical particles and make relevant observations. We also plot the local Mach number contours to explain the various observed complex physical mechanisms occurring during shock-particle interaction. Finally, since shock interaction with particles lead to transmitted and reflected waves, we compute the average pressure in the computational domain to characterize the strength of the transmitted shock wave to study pressure attenuation behind the particle barrier. By analyzing the pressure field we can determine the effect of particles on the flow.

DOI: 10.1103/PhysRevFluids.1.054202

I. INTRODUCTION

The study of shock interaction with particles is largely motivated by its extensive applications. It has wide ranging applications in environmental, industrial, and military fields. Natural phenomena such as volcanic eruption [1], meteorite breakup [2], and astrophysical phenomena such as solar flares [3] and supernovae are dominated by shock-particle interaction. Military applications include obscurant dissemination for smoke grenades, explosive dispersal of particles, and pressure attenuation by using a porous barrier for shielding objects from blast waves. Hence, because of its wide ranging applications, it is of practical importance to understand the mechanics of shock-particle interaction.

In the aforementioned phenomena, the lead or primary shock interacts with $O(10^3)$ to $O(10^9)$ or more particles. The diameter of the particles can vary from a few microns to meters and these phenomena typically occur over domains that can vary from a few millimeters to meters. If one were to study this problem and perform a numerical simulation by resolving all length and time scales, then it would require grids that are on the order of $\sim 10^{20}$ computational cells and tracking multiples of 10^9 particles. Numerical simulations of these sizes cannot be performed with currently available computational resources. To overcome this, the problem of shock interaction with particles has been studied at different scales, i.e., at the microscale (fully resolved particles) and the meso- and macroscales (point-particle models).

At the meso- and macroscales, the flow around the particles is not fully resolved. Particles are treated as subgrid points and their motion is tracked using Lagrangian dynamics, with forces described by analytical models. This approach reduces the degrees of freedom for the problem to

*Corresponding author: tlj@ufl.edu

a manageable scale and renders it numerically solvable. Extensive research has been carried out to understand shock interaction with dispersed phase to discern the underlying physical mechanisms and to develop models for predicting the particle motion and heat transfer. Saito *et al.* [4] studied the effect of unsteady force on the wave structure behind the shock wave in a gas-particle mixture, while Boiko *et al.* [5] performed numerical simulations and experiments to study shock interacting with a cloud of particles. More recently Wagner *et al.* [6,7] carried out multiphase shock tube experiments of planar shock wave propagating over a particle curtain. Ling *et al.* [8] proposed a one-dimensional (1D) analytical model to predict the motion of the particles and heat transfer for shock particle interaction. There is an inherent error associated with these models and numerical simulations since all the scales are not resolved and there are approximations involved while deriving the models. Current state-of-the-art models cannot capture the complex physical phenomena occurring during shock interacting with particles. To better understand the physical mechanisms, the problem of shock-particle interaction has been studied at the microscale.

Typical analytical models for the forces used at the meso- and macroscales are either heuristic in nature or rigorously derived for a single isolated particle at the microscale. At the microscale, spatial and temporal scales are resolved around a particle to obtain time-dependent forces and heat transfer. Over the past few decades, multiple fully resolved numerical simulations and experiments have been carried out to study shock interacting with a single isolated particle. For example, Igra and Takayama [9] performed shock tube experiments to measure the drag experienced by a spherical particle in the wake of a shock. They compared the measured drag force against the standard drag model and reported that the experimental drag force was significantly higher than the predicted drag. Britan *et al.* [10] computed the trajectory and velocity of a spherical particle in a shock tube for various particle sizes and shock Mach numbers. Tanno *et al.* [11,12] and Sun *et al.* [13] have carried out experiments using an accelerometer installed inside a spherical particle to record time-resolved measurements of the force exerted by a shock wave. Along with the experimental investigations, extensive research has been carried out for modeling shock interaction with a single isolated particle. For example, Loth [14] investigated the effect of compressibility and rarefaction on the drag experienced by a spherical particle. Parmar *et al.* [15] proposed a simple drag model and further derived an analytical equation for the motion of spherical particle [16,17] in nonuniform flows. Fedorov *et al.* [18] proposed a model for the drag and Ling *et al.* [19] highlighted the importance of unsteady forces in modeling the drag of shock-particle interaction.

There are several relevant time scales associated with shock-particle interaction problem [20]. (i) The shock-particle interaction time is defined by $\tau = d_p/u_s$, where d_p is the particle diameter and u_s is the shock speed. On this time scale the shock passes over the particle. (ii) The acoustic time scale $\tau_a = d_p/c$, where c is the speed of sound, measures the time taken for an acoustic signal to propagate over a particle diameter. (iii) The inviscid time scale $\tau_i = d_p/u_{ps}$ is based on the postshock flow velocity. On this inviscid time scale the mass-averaged particle pressure rapidly increases. Since the three velocities u_s, c, and u_{ps} are related and are of the same order, the three time scales τ, τ_a, and τ_i are also of the same order and inviscid in nature. (iv) The viscous diffusional time scale can be defined as $\tau_v = \delta_v^2/\nu_m$, where ν_m is the kinematic viscosity of the medium. Here δ_v is the boundary layer thickness, whose value for the steady postshock flow can be estimated as $\delta_v/d_p = 1/\sqrt{\mathrm{Re}}$, where the Reynolds number based on the postshock velocity is defined as $\mathrm{Re} = d_p u_{ps}/\nu_m$. (v) The traditional time scale of particle motion defined by $\tau_p = \rho_p d_p^2/18\mu_m \equiv (\rho_p/\rho_m)d_p^2/18\nu_m$ comes about by the application of Newton's second law with the force given by the Stokes drag. Here ρ_p is the particle density; ρ_m and μ_m are the density and viscosity of the medium surrounding the particle, respectively. On this time scale the particle will accelerate to the postshock gas velocity. The ratio of the particle to inertial time scales is given by $\tau_p/\tau = (\rho_p/\rho_m)(u_s/u_{ps})\mathrm{Re}/18$. Conservative values of the parameters for the current application of a shock propagating in air over a solid particle are $d_p = O(10^{-4})$ m, $\rho_p/\rho_g = O(10^3)$, $u_{ps} = O(10^2)$ m/s, and $\nu_m = O(10^{-5})$ m^2/s, giving a Reynolds number of $\mathrm{Re} = O(10^3)$. Thus, the ratio of particle to inertial time scales becomes $\tau_p/\tau = O(10^5)$. This implies that the particle motion

may not be important until the shock has traveled much farther downstream. See also the discussion in [21].

The ratio of viscous to inertial time scales is given by $\tau_v/\tau = u_s/u_{ps}$. For a shock of Mach number 1.5, $u_s/u_{ps} = 2.2$ and the ratio remains $O(1)$ as the shock Mach number varies. At any point on the surface of the sphere the viscous boundary layer starts growing after the arrival of the shock and develops on a time scale a few times larger than that shock-particle interaction time scale. Thus, during shock-particle interaction we can expect the peak force on the particle (which happens when the shock is slightly downstream of the particle center) to be dictated primarily by inertial effects and unaffected by viscous effects. However, we can expect the viscous effect to play a role once the shock has propagated two or so diameters downstream of the particle. A comparison of inviscid and viscous simulations of a planar shock propagation over an isolated particle supports the above assertion; see Fig. 6(a) of Sec. III A below. The shock-induced peak force on the particle computed from the inviscid and viscous simulations are in excellent agreement and differences between the two appear for $t > 2\tau$.

By studying shock interaction with a single isolated particle, one can obtain exact time-resolved results. In reality, however, typical shock-particle phenomena have multiple particles involved. Physical mechanisms occurring in the case of shock interaction with a single isolated particle are altered for shock interacting with a distribution of particles. Drag force on particles is greatly impacted by the presence of neighboring particles and this is not captured by the current models. Therefore, there is a need to understand the effect of neighboring particles or the effect of local volume fraction on the drag force.

Currently there is limited data on fully resolved results of shock interacting with multiple particles. For two-dimensional simulations, shock propagation over random beds of disks was carried out in [21,22]. Among a number of important findings, the authors computed the unsteady inviscid drag forces experienced by the particles as a function of Mach number and particle volume fraction. Both the transmitted and reflected waves were investigated as well as the complex wave pattern within the random bed. For three-dimensional simulations, Sridharan *et al.* [23] investigated shock interaction with a 1D array of spherical particles in air. They observed that the peak value of the unsteady inviscid drag increases and then asymptotes as the primary shock propagates through the array, depending on the shock Mach number and the particle spacing. The trend for the peak drag as a function of shock Mach number and particle separation is presented, which shows that the complex interaction of the waves in between the particles might lead to either constructive or destructive interference. This complex interaction of waves has an important effect on the peak value of drag. More recently, Mehta *et al.* [24] studied the effect of particle spacing and shock Mach number on the drag force for the case of a transverse array of particles. They compared the drag force against the drag force on a single particle to highlight the effect of neighboring particles.

To better understand the complex problem of shock interaction with multiple randomly distributed particles, we carry out three-dimensional inviscid simulations and investigate the limiting case, that of a primary shock interacting with a three-dimensional structured face centered cubic (fcc) array of particles. As argued earlier, the present inviscid simulations will accurately capture the peak and the short time evolution of the force on the different particles. However, the evolution of the flow and the force on the particles, once the shock is past a couple of particle diameters, will be influenced by viscous boundary layer development. We plot the nondimensional drag for the fcc array of particles and compare it against the results from Sridharan *et al.* [23]. We also isolate the effect of volume fraction and shock Mach number on the drag force on the particles by comparing the force history with that of a single particle. We explain the various observed physical mechanisms occurring during shock interaction with particles by plotting the local Mach number contours for different cases.

Finally, we compute the average streamwise pressure along the computational domain to characterize the strength of the transmitted shock. Such characterizations are important to understand in a number of physical situations. For example, one of the major security applications of shock interaction with particles is pressure attenuation behind porous barriers to shield objects from adverse pressure originating from a blast wave. Extensive research has been carried out in this field because

of its obvious importance. In the case of shock interaction with particles, a transmitted shock wave travels downstream through the particles and a reflected wave travels upstream. It is important to characterize the strength of these waves to understand the effect of particles on the flow. Suzuki *et al.* [25] investigated pressure attenuation behind a cylindrical array in the scenario of a blast wave propagating through the array. They performed experiments and reported the loss of pressure for the transmitted shock for various configurations of the array. Chaudhuri *et al.* [26] performed numerical simulations to study shock interaction with solid obstacles and investigated the effect of geometry on the pressure attenuation of the transmitted shock wave behind the obstacles. Rogg *et al.* [27] performed experiments and Epstein *et al.* [28] conducted simulations of shock propagating through cylindrical and spherical barriers and reported pressure attenuation for the transmitted shock wave. Naiman *et al.* [29] performed numerical simulations of planar shock interacting with a cylindrical barrier and investigated the effect of porosity on the transmitted shock wave. They reported pressure amplification behind the barrier, suggesting that in certain scenarios porous barriers will have an adverse effect on the objects that the barrier is supposed to shield from the high pressure of the blast wave.

This paper is organized as follows. The governing equations, numerical method, method for computing the drag force, simulation setup, and grid resolution study are presented in Sec. II. The results are presented in Sec. III. Here we compute the unsteady inviscid drag as a function of volume fraction and shock Mach number and plot local Mach number contours to explain the various observed complex physical mechanisms occurring during shock-particle interaction. We also investigate the pressure attenuation behind the fcc array of particles. Finally, a summary is given in Sec. IV.

II. BASIC MODEL

A. Governing equations

In this paper we focus on the early time behavior of shock-particle interaction, where the interaction is dominated by inviscid mechanisms and so viscous and thermal effects are ignored. The appropriate dimensional equations governing an inviscid fluid are therefore given by

$$\frac{\partial \rho}{\partial t} + \vec{\nabla} \cdot (\rho \vec{u}) = 0, \tag{1}$$

$$\frac{\partial (\rho \vec{u})}{\partial t} + \vec{\nabla} p + \vec{\nabla} \cdot (\rho \vec{u} \vec{u}) = 0, \tag{2}$$

$$\frac{\partial E}{\partial t} + \vec{\nabla} \cdot [(E + p)\vec{u}] = 0, \tag{3}$$

where ρ is the density, $\vec{u} = (u, v, w)$ the velocity, p the pressure, and E the total energy per unit volume. The total energy is given by

$$E = \rho\left(e + \tfrac{1}{2}\vec{u} \cdot \vec{u}\right), \tag{4}$$

where e is the internal energy. The system is closed once an equation of state $p = p(\rho, e)$ is chosen. In this work we assume an ideal gas for air with properties $\gamma = 1.4$, $c_p = 1004.6$ J/kg K, and $R = 287.04$ J/kg K.

B. Numerical method

The Euler equations are solved using a finite-volume solver on a body-conforming unstructured grid. A second-order accurate AUSM+ [30] scheme is used for flux computation and the gradients are modified using a weighted essentially nonoscillatory reconstruction technique [31]. Time integration is performed using a strong-stability-preserving third-order Runge-Kutta method. This code has been

tested and validated previously for numerous problems involving compressible flows with shock waves. Validation and verification of the numerical scheme can be found in Ref. [32].

In the current simulations the particles are held fixed in space. The short-lived transient force created as the shock interacts with the particle imparts a nearly impulsive force on the particle. If the particle were allowed to freely move, as shown by Ling *et al.* [20], the ratio of change in particle velocity due to this impulsive force to that of fluid velocity across the shock scales as a fluid-to-particle density ratio. In the present case of an aluminum particle in air, the density ratio is $O(1000)$ and the initial impulsive gain in particle velocity is small. The time scale associated with significant particle movement is therefore relatively long due to the large inertia of the particle (the particle-fluid density ratio is large). Thus, for the situation and time scales considered here, it is reasonable to ignore particle movement.

C. Drag

The drag coefficient is defined by

$$\vec{C}_D = \frac{\vec{F}}{\frac{1}{2}\rho_{ps} u_{ps}^2 A}, \tag{5}$$

where $\vec{F}$ is the force, ρ_{ps} is the postshock density, u_{ps} is the corresponding postshock speed, and A is the projected area of the particle. For a sphere, $A = \pi d_p^2/4$, where d_p is the particle diameter. Note that since we are carrying out inviscid simulations, only the pressure contributes to the force. The force components are therefore given by

$$F_i = \vec{F} \cdot \hat{e}_i \equiv \int_{S_p} p\hat{n} \cdot \hat{e}_i dS, \tag{6}$$

where $\hat{e}_i$ is the unit vector in the x_i direction, $\hat{n}$ is the outward pointing normal, and S_p is the surface of the particle. In this way the drag coefficients in the x, y, and z directions are given by

$$C_D = \frac{F_x}{\frac{1}{2}\rho_{ps} u_{ps}^2 A}, \quad C_{L,y} = \frac{F_y}{\frac{1}{2}\rho_{ps} u_{ps}^2 A}, \quad C_{L,z} = \frac{F_z}{\frac{1}{2}\rho_{ps} u_{ps}^2 A}. \tag{7}$$

The total drag coefficient is given by $C_{D,T}^2 = C_D^2 + C_{L,y}^2 + C_{L,z}^2$. We note that for a single particle $C_{L,y} = C_{L,z} = 0$ and therefore the total drag is just the drag coefficient in the streamwise direction, namely, $C_{D,T} = C_D$. This is also true for the fcc array considered here, in that the lift forces are zero by symmetry.

D. Geometry, simulation setup, and boundary conditions

In this paper we consider particles arranged in a face centered cubic cell. Figure 1(a) is an illustration of a single fcc unit cell, where particles marked as 1 are at the eight vertices of the cube, while particles marked as 2 reside on the six faces of the cube. Figure 1(b) shows the simulation domain. We have two unit cells in the simulation domain and thus there are 23 unique particles, for a total of ten complete spheres. Figure 2 shows the distribution of the particles in the simulation domain. On planes 1, 3, and 5, the computational domain includes a full sphere at the center and four quarter spheres at the corners, for a total of six spheres. On planes 2 and 4, the computational domain includes four half spheres on the sides, for a total of four spheres. This, along with symmetry boundary conditions along the y and z directions, corresponds to a unit cell in the y-z plane for the fcc arrangement. A primary or genesis shock is initialized upstream of the particles and travels downstream in the positive x direction. Once the primary shock has reached plane 1, a transmitted shock propagates through the array, while a reflected wave travels upstream. If the postshock Mach number is supersonic, the reflected wave will be a shock. The domain is periodic in the transverse (y-z) directions.

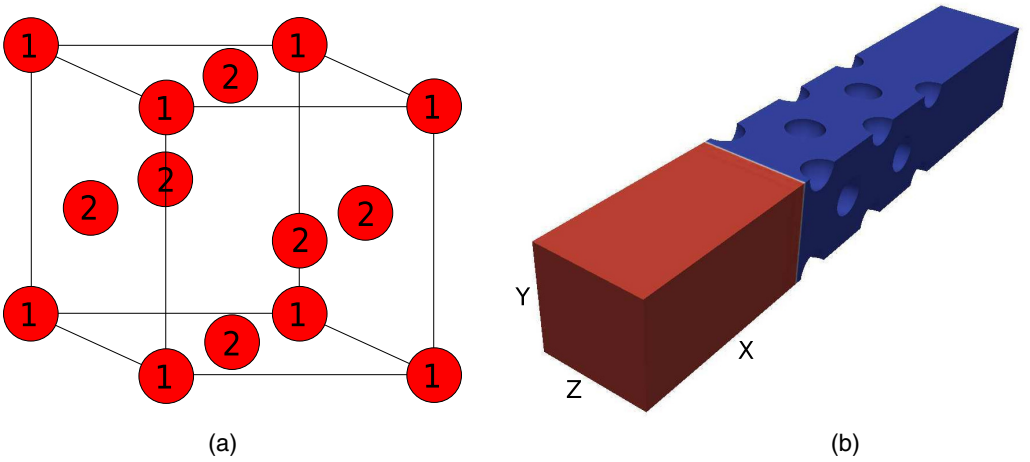

FIG. 1. (a) Representation of a fcc unit cell. (b) Plot of the three-dimensional simulation domain.

Since we are solving the inviscid equations, there are only two relevant length scales in the problem, the particle diameter and the spacing between the particles. These two length scales can be grouped into a single parameter, the volume fraction. The volume fraction ϕ is defined by

$$\phi = \frac{\text{volume of particles}}{\text{volume of unit cell}}. \tag{8}$$

Here the length L of the simulation domain in the transverse (y and z) directions is fixed at 1 unit and so the volume fraction is varied by changing the diameter of the spherical particles; Table I gives the nondimensional diameters as a function of volume fraction ϕ.

To investigate the effect of the primary shock Mach number and volume fraction on the inviscid unsteady forces, multiple simulations are performed by varying the primary shock Mach number M_s and volume fraction ϕ; see Table II for the simulation matrix. We consider primary shock Mach numbers M_s from 1.5 to 6 and volume fractions from 10% to 40%.

The preshock state is quiescent ambient air with $P = 101\,325$ Pa and $\rho = 1.2048$ kg/m^3. Table III gives the postshock conditions for air as determined by the Rankine-Hugoniot relations. Note from the table that the Mach number of the postshock uniform flow M_{ps} becomes supersonic as the primary shock Mach number M_s increases; the critical Mach number in the postshocked state for a steady secondary shock to appear around an isolated sphere is about $M_{ps} \approx 0.6$. As M_{ps} increases above 1.0 the secondary shock moves upstream of the particle and forms a bow shock. Note also from the table that the postshock pressure p_{ps} in air remains well below the yield strength for most materials ($Y \approx 0.2$ GPa) and so we do not expect the particles to deform.

FIG. 2. (a) The x-y cut section of the simulation domain at $z = 0$ and (b) isometric view of the simulation domain showing the distribution of particles in the y-z planes.

TABLE I. Values of nondimensional diameters $\mathcal{D}$ of spherical particles for different volume fractions.

Volume fraction ϕ	$\mathcal{D}/L$
10%	0.3628
20%	0.4571
30%	0.5232
40%	0.5759

The simulation domain length in the streamwise x direction varies according to the values of the primary shock Mach number and volume fraction so as to avoid disturbances or reflections from upstream and downstream boundaries, which can affect the flow field around the particles. The left boundary is treated as a constant inflow boundary with inflow at postshock properties, while all other boundaries, including the particle surfaces, are treated as slip walls.

E. Grid resolution

Unstructured tetrahedral grids are used for carrying out the fully resolved three-dimensional simulations. GRIDPRO [33] is used to create the surface mesh of the simulation domain. This surface mesh is then used as an input to TETGEN [34], which generates the body-conforming unstructured tetrahedral mesh inside the simulation domain. The quality and size of the elements in the domain determine the sharpness of the shock and the accuracy of the solution. Similarly, adequate mesh resolution on the particle surface is required to properly compute particle forces, which are determined by integrating flow properties on the surface of each particle. The quality and size of the elements are controlled by monitoring the element aspect ratio and maximum element volume. Surface mesh resolution is controlled by specifying the maximum element area. A grid resolution study is performed to determine the effect of these two constraints, the size of the elements in the domain, and the surface mesh resolution per particle, on the solution. RUN1 from Table II with volume fraction $\phi = 10\%$ and shock Mach number $M_s = 1.5$ is selected for the grid resolution study. For this case, a matrix of simulations is performed by varying the surface mesh per particle from 43 000 elements to 110 000 elements. The total volume mesh is varied from 6×10^6 to 30×10^6 elements. See Table IV for a list of the simulation runs used in the grid resolution study. Here RES1 represents the finest grid and RES25 represents the coarsest grid. A typical computational mesh is shown in Fig. 3.

Results of the grid resolution study are presented in Fig. 4. Figure 4(a) plots the drag coefficient for the center particle of plane 3 as a function of nondimensional time t/τ, where τ is the shock-particle interaction time defined in the Introduction. In the figure we only present results for those simulations that best represent the entire matrix of simulations from Table IV. From the figure we note how well the various resolutions capture the drag coefficient. To better quantify the numerical error, we identify in Fig. 4(a) three instances of the unsteady drag history. Instance 1 ($\tilde{t_1} = t_1/\tau = 3.313$)

TABLE II. Matrix of simulations.

ϕ	$M_s = 1.5$	$M_s = 2.0$	$M_s = 3.0$	$M_s = 6.0$
10%	RUN1	RUN2	RUN3	RUN4
20%	RUN5	RUN6	RUN7	RUN8
30%	RUN9	RUN10	RUN11	RUN12
40%	RUN13	RUN14	RUN15	RUN16

TABLE III. Values of primary shock Mach number M_s; postshock pressure p_{ps}; density ρ_{ps}; velocity u_{ps}; Mach number $M_{ps} = u_{ps}/c_{ps}$, where $c_{ps} = \sqrt{\gamma p_{ps}/\rho_{ps}}$ is the speed of sound in the postshock state; and shock velocity u_s.

Case	M_s	p_{ps} (10^5 Pa)	ρ_{ps} (kg/m^3)	u_{ps} (m/s)	M_{ps}	u_s (m/s)
1	1.5	2.49	2.2422	238.3514	0.60	514.8390
2	2.0	4.55	3.2111	429.0325	0.96	686.4520
3	3.0	10.47	4.6446	762.7244	1.36	1029.6780
4	6.0	42.39	6.3439	1668.4597	1.73	2059.3560

is just after the shock has interacted with the particle, instance 2 ($\tilde{t}_2 = t_2/\tau = 3.5$) corresponds to the peak drag, and instance 3 ($\tilde{t}_3 = t_3/\tau = 4.7$) corresponds to a time after the shock has left the particle. Expanded views of these three instances are plotted in Figs. 4(b)–4(d), respectively. Table V summarizes the grid resolution study. The table gives values of C_D at the three different instances shown in Fig. 4(a). Since RES1 is the finest grid, we compute the relative error for all other simulations compared to RES1. For example, the relative error $\mathcal{E}_{\text{rel}}$ at instance 1 for RES2 is given by

$$\mathcal{E}_{\text{rel}} = \frac{|C_D(\tilde{t}_1,\text{RES1}) - C_D(\tilde{t}_1,\text{RES2})|}{|C_D(\tilde{t}_1,\text{RES1})|} \times 100. \tag{9}$$

Keep in mind that we need to optimize the grid so as to minimize the computational cost while at the same time obtain a grid independent solution. We establish that RES13 has roughly 1% error or less when compared to the finest grid resolution. We choose this grid resolution for carrying out the matrix of simulations given in Table II. Since the domain size varies according to volume fraction, the total number of elements also varies. Table VI provides the final information for the grid resolution for the simulation matrix of Table II.

To check the validity of the grid resolution of RES13 for a higher Mach number and volume fraction, we performed one more simulation for the case of $\phi = 30\%$ and $M_s = 6.0$ (RUN12 of Table II). We call this grid resolution the coarse grid. In addition to this resolution, we generated another grid with 151 000 elements on the surface of each particle, for a total of 28×10^6 elements in the computational domain; we call this the fine grid. Results are presented in Fig. 5. We quantify the relative error for the coarse grid compared to the fine grid at three instances. Instance 1 ($\tilde{t}_1 = t_1/\tau = 2.45$) is just after the shock has interacted with the particle, instance 2 ($\tilde{t}_2 = t_2/\tau = 2.6$) corresponds to the peak drag, and instance 3 ($\tilde{t}_3 = t_3/\tau = 3.63$) corresponds to a time after the shock has left the particle. We note that the relative error at all three instances is less than 1%.

In summary, we conclude that the grid resolution of RES13 can be used for all shock Mach numbers and volume fractions while minimizing the numerical error and the computation cost.

TABLE IV. Matrix of simulations for grid resolution study corresponding to RUN1 of Table II. Columns denote the total number of elements in the domain ($\times 10^6$), while rows denote the number of surface elements on each particle.

Surface \ Volume	30×10^6	22×10^6	18×10^6	13×10^6	6×10^6
110 000	RES1	RES2	RES3	RES4	RES5
82 000	RES6	RES7	RES8	RES9	RES10
70 000	RES11	RES12	RES13	RES14	RES15
57 000	RES16	RES17	RES18	RES19	RES20
43 000	RES21	RES22	RES23	RES24	RES25

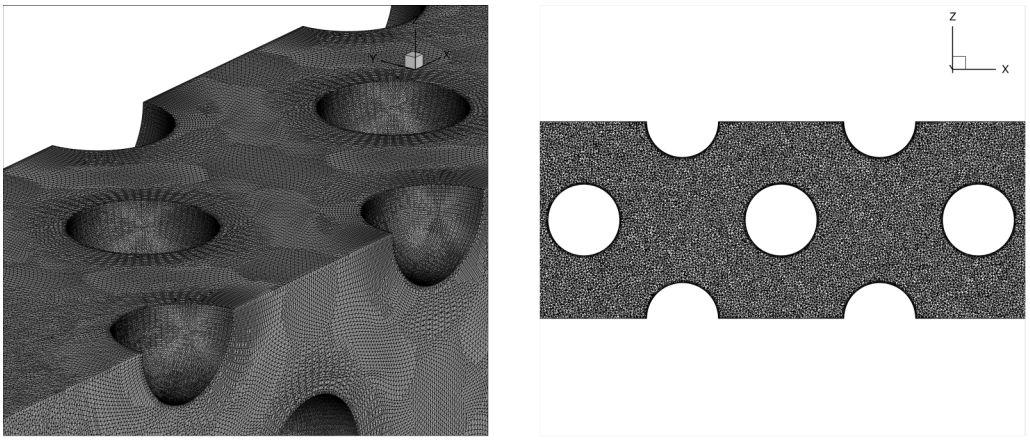

FIG. 3. Computational mesh corresponding to RES13: (a) three-dimensional view and (b) $y = 0$ cut.

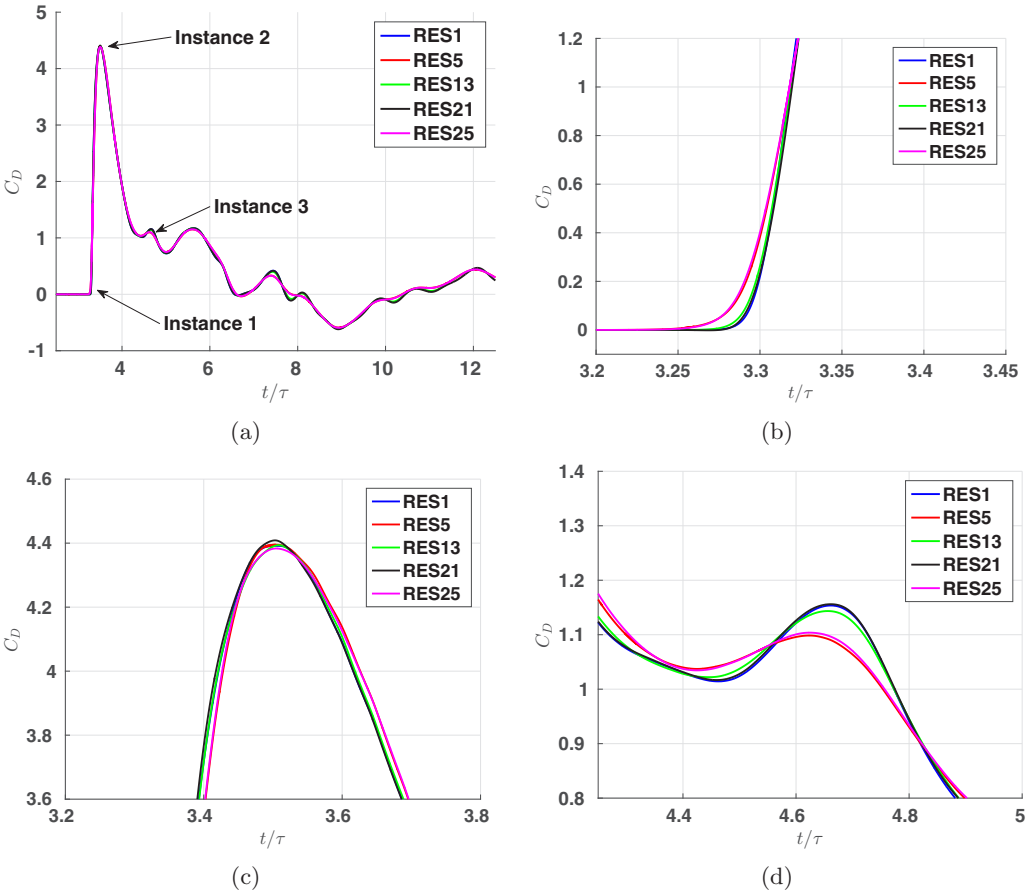

FIG. 4. (a) Plot of the drag coefficient C_D as a function of nondimensional time t/τ for resolutions RES1 (blue), RES5 (red), RES13 (green), RES21 (black), and RES25 (magenta). Also shown is the enhanced view of the three instances shown in (a): (b) instance 1 ($\tilde{t}_1 = t_1/\tau = 3.313$), (c) instance 2 ($\tilde{t}_2 = t_2/\tau = 3.5$), and (d) instance 3 ($\tilde{t}_3 = t_3/\tau = 4.7$).

TABLE V. Values of C_D and relative error (in percent) at instances 1–3.

Simulation	$C_D(\tilde{t}_1)$	$C_D(\tilde{t}_2)$	$C_D(\tilde{t}_3)$	Error at $\tilde{t}_1$	Error at $\tilde{t}_2$	Error at $\tilde{t}_3$
RES1	0.7202	4.3914	1.1365	0	0	0
RES2	0.7256	4.4038	1.1266	0.76	0.28	0.87
RES3	0.7379	4.3892	1.1163	2.46	0.05	1.78
RES4	0.7364	4.3878	1.1088	2.26	0.08	2.44
RES5	0.7950	4.3951	1.0637	10.38	0.08	6.41
RES6	0.7242	4.4017	1.1356	0.56	0.23	0.08
RES7	0.7266	4.3975	1.1291	0.89	0.14	0.65
RES8	0.7609	4.3876	1.1202	5.66	0.09	1.44
RES9	0.7413	4.3830	1.1099	2.93	0.19	2.35
RES10	0.8354	4.3936	1.0747	15.99	0.05	5.44
RES11	0.7031	4.4039	1.1381	2.38	0.28	0.14
RES12	0.7169	4.4013	1.1271	0.46	0.22	0.83
RES13	0.7236	4.3935	1.1241	0.48	0.05	1.10
RES14	0.7223	4.3890	1.1096	0.30	0.05	2.36
RES15	0.8104	4.3799	1.0740	12.53	0.26	5.50
RES16	0.6792	4.4039	1.1376	5.69	0.28	0.09
RES17	0.6844	4.3990	1.1317	4.98	0.17	0.43
RES18	0.7031	4.3910	1.1242	2.37	0.01	1.09
RES19	0.7182	4.3835	1.1106	0.28	0.18	2.28
RES20	0.7998	4.3922	1.0767	11.05	0.02	5.26
RES21	0.6730	4.4086	1.1388	6.56	0.39	0.20
RES22	0.6749	4.3961	1.1307	6.28	0.11	0.51
RES23	0.6642	4.3918	1.1241	7.78	0.01	1.10
RES24	0.6991	4.3810	1.1151	2.93	0.24	1.89
RES25	0.8033	4.3833	1.0702	11.53	0.19	5.84

III. RESULTS

In this section we present results for a shock propagating over a fcc array. We first carry out inviscid simulations for a single spherical particle. This is the limiting case of the fcc array with volume fraction tending to zero. For this case we study the effect of shock Mach number on the force history. We next carry out three-dimensional inviscid simulations of shock propagating over a fcc array of particles to study the effect of volume fraction and shock Mach number. We make relevant comparisons for the force history on the fcc array of particles against the force history on a single particle, as well as the force history on a one-dimensional structured array of particles given by

TABLE VI. Grid resolution for the simulation matrix of Table II. The second column lists the number of surface elements on each particle, while the third column lists the total number of elements in the computational domain.

Volume fraction ϕ	Surface	Volume
10%	70 000	18×10^6
20%	109 000	21×10^6
30%	144 000	22×10^6
40%	81 000	22×10^6

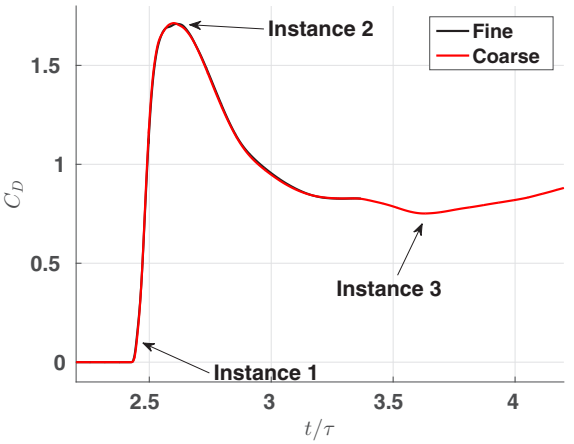

FIG. 5. Plot of drag coefficient C_D as a function of nondimensional time t/τ for $\phi = 30\%$ and $M_s = 6.0$: fine grid (black) and coarse grid (red).

Sridharan *et al.* [23]. Finally, we compute the average streamwise pressure along the computational domain to characterize the strength of the transmitted shock.

A. Single particle

We consider the limiting case of the fcc array with zero volume fraction and study the effect of shock Mach number on the drag coefficient. Results are presented in Fig. 6. Figure 6(a) plots the drag coefficient as a function of nondimensional time for shock Mach number $M_s = 1.22$. Also shown in the figure is the experimental data (red) and results from viscous simulations (black) from [13]. Note that the results of the viscous and inviscid simulations begin to deviate around $t/\tau = 2$. This is consistent with the time scale analysis presented in the Introduction, in that viscous effects only become important when the shock has propagated about a particle diameter downstream of the

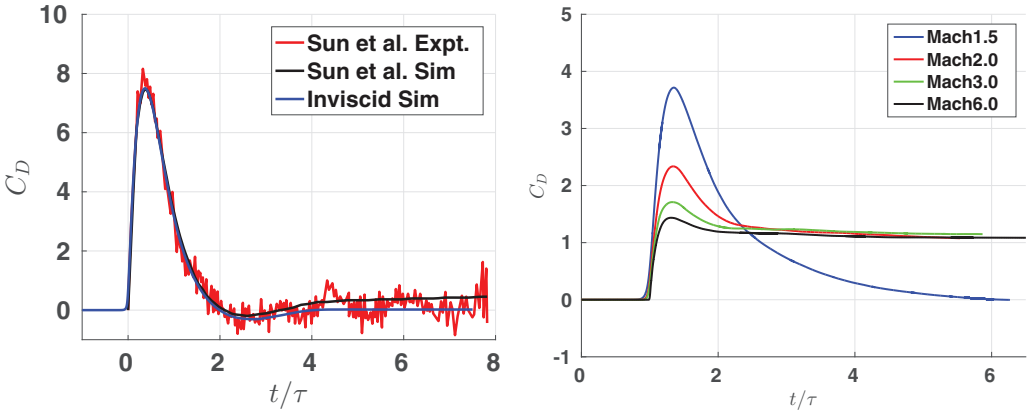

FIG. 6. (a) Plot of the drag coefficient as a function of nondimensional time for $M_s = 1.22$. Here the experimental data (red) and viscous simulation (black) are from [13] and the inviscid simulation (blue) is from the present work. (b) Plot of the drag coefficient as a function of nondimensional time for various shock Mach numbers. Here $M_s = 1.5$ (blue), 2.0 (red), 3.0 (green), and 6.0 (black).

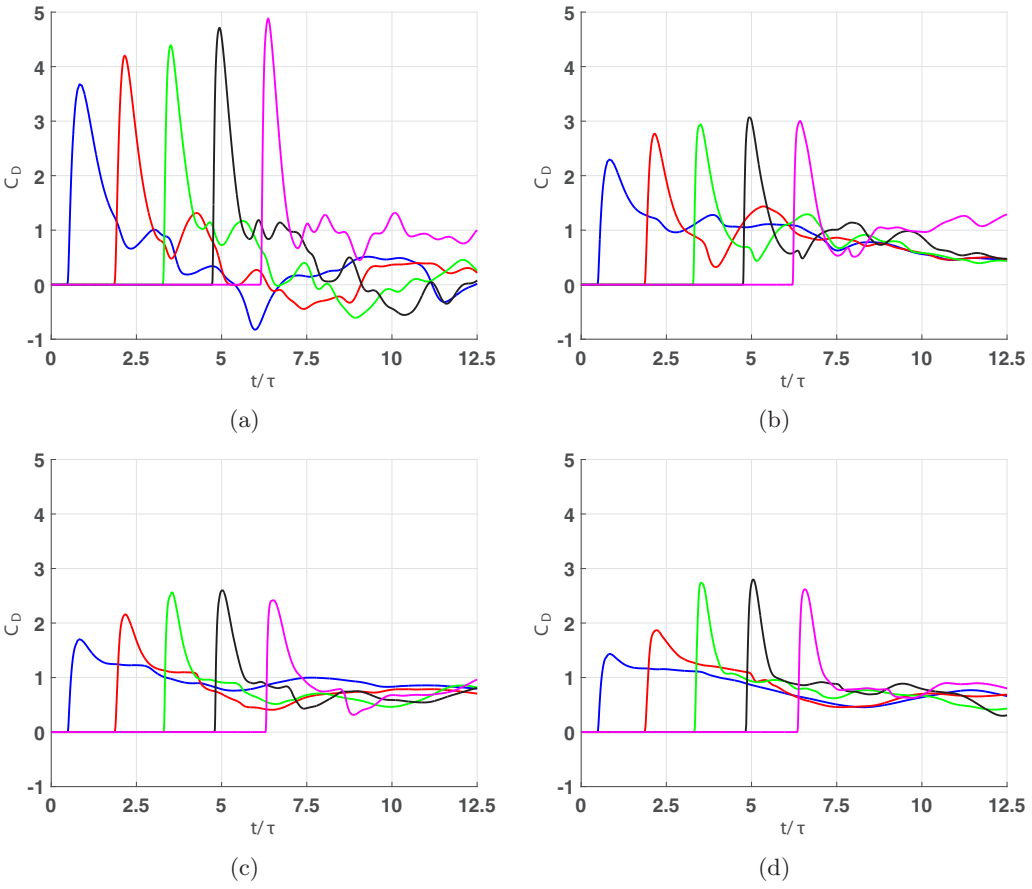

FIG. 7. Plot of the drag coefficient C_D as a function of nondimensional time t/τ for $\phi = 10\%$ and (a) $M_s = 1.5$, (b) $M_s = 2.0$, (c) $M_s = 3.0$, and (d) $M_s = 6.0$. Colors correspond to plane 1 (blue), plane 2 (red), plane 3 (green), plane 4 (black), and plane 5 (magenta).

particle. Thus, inviscid simulations properly capture the peak drag coefficient and the early time behavior of the drag history. Figure 6(b) plots the drag coefficient as a function of nondimensional time for various shock Mach numbers. From the figure we see that the peak value C_D decreases as the shock Mach number increases by virtue of the scaling (5) using postshock reference values. This result is consistent with those presented in [23,24,35]. Also note from the figure that C_D for $M_s = 1.5$ goes to zero after $t/\tau \sim 6$. This is because the postshock Mach number from Table III is subcritical and therefore we do not expect a secondary shock associated with the postshock flow around the particle. On the other hand, for $M_s = 2.0$, 3.0 and 6.0, M_{ps} is above the critical value for a sphere. This results in the formation of a secondary shock either around or in front of the particle and hence there is a nonzero steady wave drag experienced by the particle. The limiting value is approximately 1.1, which is consistent with experiments [36,37] and numerical fits [14,38].

B. The fcc array of particles

1. Drag coefficient

The unsteady drag coefficients for shock propagating through a three-dimensional fcc array of particles are presented in Figs. 7–10. Here the drag coefficients, as calculated from Eqs. (6) and (7),

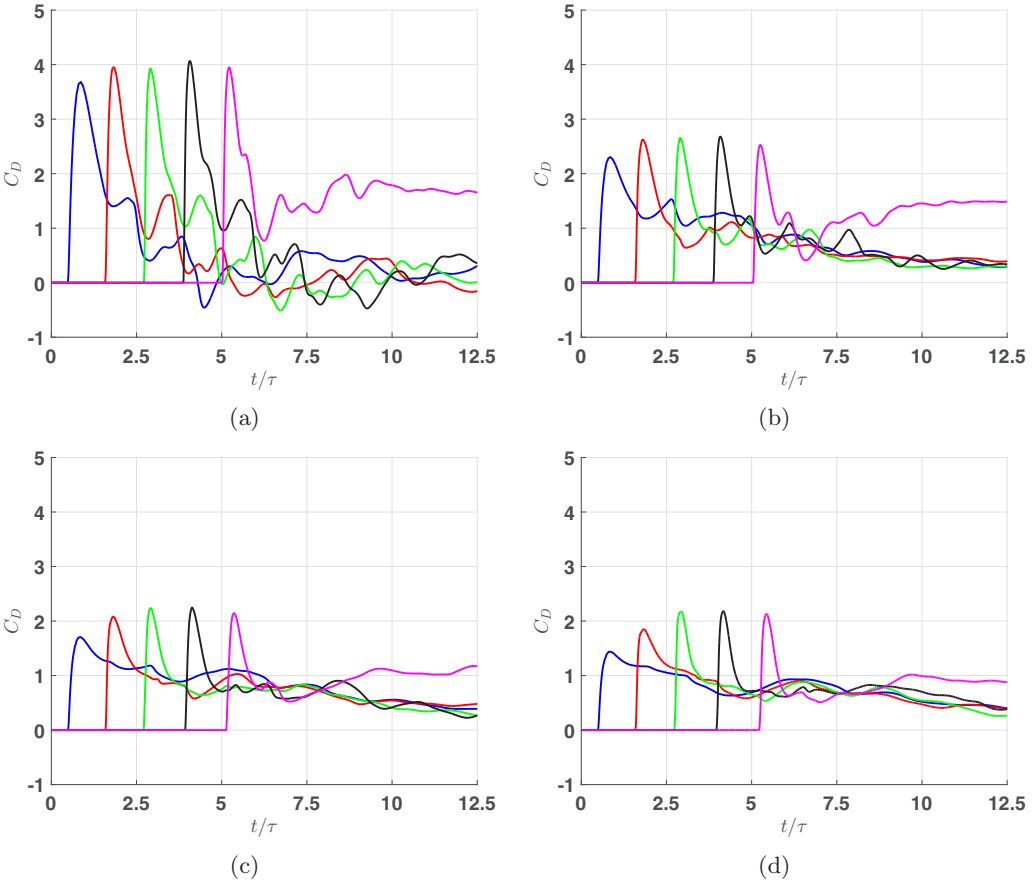

FIG. 8. Plot of the drag coefficient C_D as a function of nondimensional time t/τ for $\phi = 20\%$ and (a) $M_s = 1.5$, (b) $M_s = 2.0$, (c) $M_s = 3.0$, and (d) $M_s = 6.0$. Colors correspond to plane 1 (blue), plane 2 (red), plane 3 (green), plane 4 (black), and plane 5 (magenta).

are plotted as a function of nondimensional time for different volume fractions and primary shock Mach numbers, which are varied according to the matrix of simulations from Table II. Since the fcc array is periodic, it is sufficient to only consider planes 1–5 as depicted in Fig. 2. Also, since the normal shock is propagating in the positive x direction, the nondimensional time axis can also be thought of as the streamwise x axis. This helps visualize the variations of C_D as a function of time and streamwise location.

Figure 7 plots C_D as a function of t/τ for different shock Mach numbers and for a fixed volume fraction of $\phi = 10\%$. For $M_s = 1.5$ [Fig. 7(a)] we observe that the peak value of C_D monotonically increases as the transmitted shock propagates through the fcc array of particles, although one cannot conclude if the peak value of C_D has asymptoted. We note that the peak drag for plane 1 is identical to that of an isolated particle. At this early time the flow around each of the first row of particles has not been influenced by its neighbors. However, after a short time, the force on the first row deviates from the force history of an isolated particle shown in Fig. 6, which can be considered as the collective influence of the neighbors. Note that the peak value has increased by about 32% going from the first plane to the fifth plane. The observation that the peak value of C_D increases as the shock propagates downstream is consistent with the findings of Sridharan *et al.* [23] for a one-dimensional array of particles. In addition to the peak increasing, we also observe fluctuations in C_D at later times. These fluctuations are the result of wave reflections from neighboring particles on each other. Negative

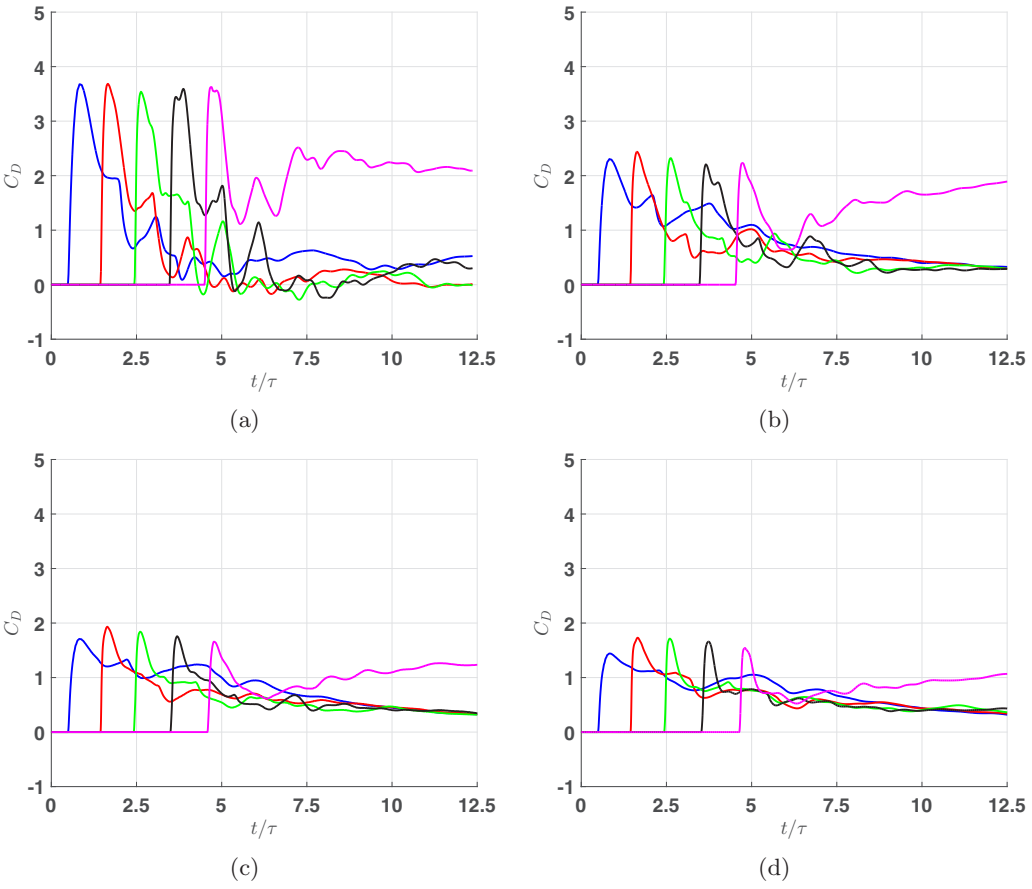

FIG. 9. Plot of the drag coefficient C_D as a function of nondimensional time t/τ for $\phi = 30\%$ and (a) $M_s = 1.5$, (b) $M_s = 2.0$, (c) $M_s = 3.0$, and (d) $M_s = 6.0$. Colors correspond to plane 1 (blue), plane 2 (red), plane 3 (green), plane 4 (black), and plane 5 (magenta).

values of C_D imply that the particle experiences a force in the direction opposite to the flow and this emphasizes the importance of unsteady force contribution that depends on the instantaneous relative acceleration between the particle and the ambient flow. Also, the negative force is due to the fact that there is focusing of the defracted shock in the wake of the particle contributing to temporary high pressure in the wake. Note that for planes 1–4, the average value of the postshock C_D for particles is close to zero. In contrast, particles in plane 5 [magenta curve of Fig. 7(a)] experience a nonzero longer-term drag because there are particles in the y-z plane upstream of it, but none downstream of it. Such differences in the long-time behavior of the force on the different planes of particles can offer a possible explanation for why planar particle curtains have been observed to substantially expand in thickness when subjected to a planar shock. That is, had the particles been allowed to move, the particles in the last plane would tend to move away from the group of particles that makes up planes 1–4. Once the last layer peels off the proceeding layer, the proceeding now becomes the last and it too peels off. This process continues resulting in a streamwise expansion of a curtain of particles. This spreading of the particle curtain is observed experimentally [6,7] and numerically [8].

Similar results are shown in Figs. 7(b)–7(d) for $M_s = 2.0$, 3.0, and 6.0, respectively. For these cases, the primary postshock Mach number is in the supercritical regime, meaning that a bow shock appears at least temporarily in front of the lead particles of plane 1. In contrast to the results for the subcritical case of $M_s = 1.5$, the peak drag increases but then begins to decrease by the fifth

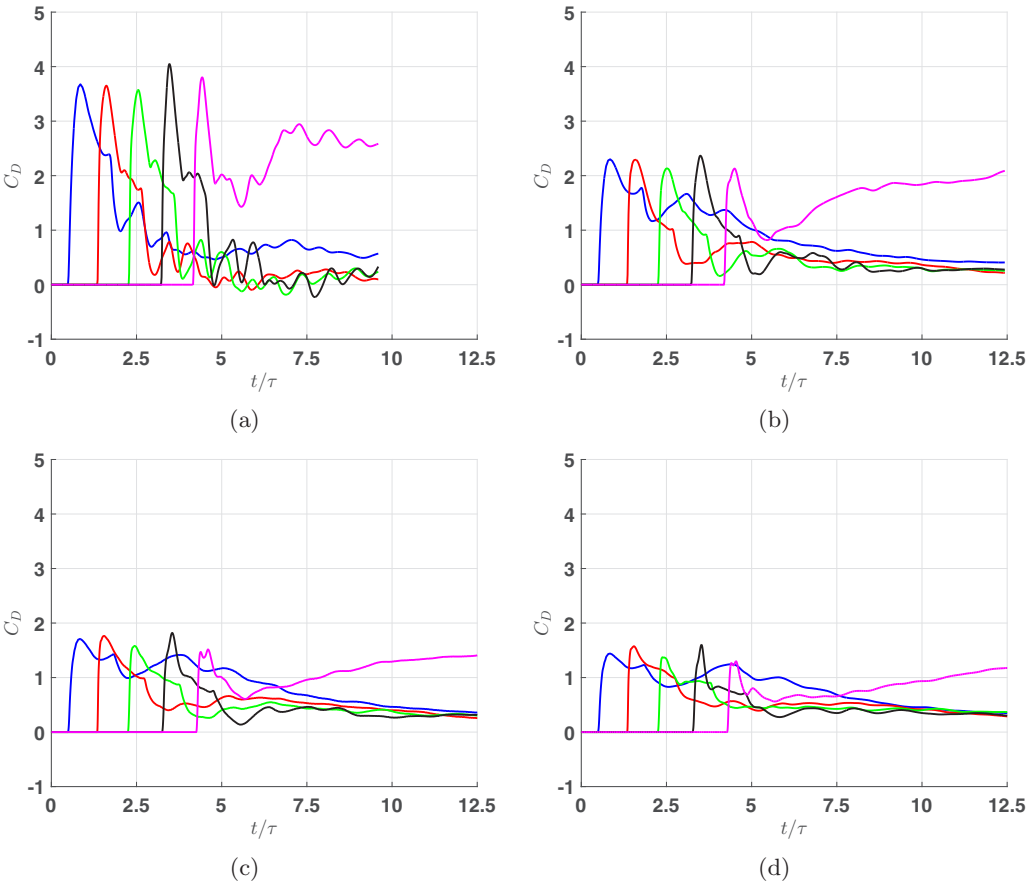

FIG. 10. Plot of the drag coefficient C_D as a function of nondimensional time t/τ for $\phi = 40\%$ and (a) $M_s = 1.5$, (b) $M_s = 2.0$, (c) $M_s = 3.0$, and (d) $M_s = 6.0$. Colors correspond to plane 1 (blue), plane 2 (red), plane 3 (green), plane 4 (black), and plane 5 (magenta).

plane. This is due to the fact that the transmitted shock weakens because of dissipation of energy by the collective secondary shocks formed in front of each y-z plane of particles. Also, as the shock Mach number increases, the difference between the peak in the first plane and the fourth plane also increases. For example, for $M_s = 2.0$, there is an increase in peak drag of about 33%, while for $M_s = 6.0$, there is almost a 94% increase in peak drag. This is consistent with Sridharan *et al.* [23], who showed that for a one-dimensional array of particles, as the shock Mach number increases, the amplification of peak drag also increases. Also, in sharp contrast to the subcritical case, the fluctuations in C_D at late times do not become negative but remain positive. We note that the averaged asymptotic value of C_D for late times lies below 1.1, the value corresponding to a single particle; e.g., compare Fig. 7(d) to the corresponding Mach number drag curve of Fig. 6. Furthermore, the averaged asymptotic value for each of the five planes are roughly equal. This suggests, at least for the times reported here, the group of particles would tend to remain tightly packed and not spread as in the $M_s = 1.5$ case. Finally, we note that the decrease in peak C_D for the particles in plane 5 is not observed for the one-dimensional array of particles studied in Sridharan *et al.* [23] and thus highlights the back effect of the array of particles in attenuating the shock wave, which becomes important when considering three-dimensional effects.

Figure 8 plots C_D as a function of t/τ for different primary shock Mach numbers and for a fixed volume fraction of $\phi = 20\%$. For $M_s = 1.5$ [Fig. 8(a)] we do not observe the same trend for the

peak value of C_D as seen in the earlier case of $\phi = 10\%$ [cf. Fig. 7(a)]. Here it can be observed that the peak value of C_D alternates between increasing and decreasing values. Since the volume fraction is higher for this case compared to the earlier one, the particles are closer to each other and hence the separation distance between them is smaller. This results in alternating constructive and destructive interference of the waves assisted by strong three-dimensional effects. As in the lower-volume-fraction case, the average value of the postshock value of C_D for particles in planes 1–4 is close to zero, while that for plane 5 [magenta curve of Fig. 8(a)] experiences a nonzero quasisteady drag. The mean, however, is significantly higher; i.e., for $\phi = 10\%$ the mean drag for plane 5 is just below 1.1, while for $\phi = 20\%$ the mean value is about 1.7. Again, had the particles been allowed to move, the particles in the last plane would tend to move away from the group of particles that makes up planes 1–4, thus leading to a spreading of the particle curtain. For the supercritical cases of $M_s = 2.0$, 3.0 and 6.0, the figure shows a trend similar to that for the case of $\phi = 10\%$, respectively. However, the peak drag of the fourth plane is lower that the corresponding value for the $\phi = 10\%$ case. For example, by comparing Fig. 8(d) to Fig. 7(d) for $M_s = 6.0$, the peak drag is about 22% lower.

Figures 9 and 10 plot C_D as a function of t/τ for different primary shock Mach numbers and for volume fractions of $\phi = 30\%$ and 40%, respectively. For $M_s = 1.5$ we observe a completely different behavior for the peak values of C_D when compared to the earlier cases of $\phi = 10\%$ and 20%. In particular, the peak value of C_D decreases until plane 3 and then either increases or oscillates. For these higher volume fractions, the particles are quite close to each other. This might cause the formation of venturilike structures and may result in nozzling or acceleration of the shock, and is responsible for the variations in peak value of C_D for particles in planes 4 and 5. In addition, the postshock drag for plane 5 increases with increasing volume fraction; i.e., for $\phi = 30\%$ the long-time mean drag is approximately 2.1, while for $\phi = 40\%$ it is 2.5. This trend indicates that the end of the particle bed will tend to move faster and farther away from the rest of the bed in time as the volume fraction increases. For $M_s = 2.0$, 3.0 and 6.0 we observe that the peak value of C_D increases from plane 1 to plane 2, but then starts decreasing or oscillating thereon. This is clearly due the effect of the higher volume fraction.

We summarize the results of all 16 simulations in Fig. 11, where we plot the peak C_D as a function of primary shock Mach number and for different volume fractions, at the five different planes. For plane 1 the peak C_D does not vary with volume fraction since it occurs when the shock has propagated 3/4 over the particle and therefore the particles in plane 1 do not experience the effect of other particles during this early time. However, as one moves downstream through the array from plane 2 to plane 5, the effect of increasing the volume fraction is to decrease the drag at a fixed shock Mach number. Such information is critical in developing the next-generation point-force particle models that can be used in simulations at the meso- and macroscales.

2. Mach contours

The nondimensional force was plotted as a function of nondimensional time in Figs. 7–10 and for different shock Mach numbers and volume fractions. Some of the force plots show similar, well-organized trends, as observed by Sridharan *et al.* [23], while in other cases there are new or different trends or there is no observable pattern. These distinct and divergent observations from the unsteady force histories highlight the complex nature of a shock propagating through a fcc array, along with the influence of shock Mach number and the volume fraction on the force experienced by the particles.

As the shock travels over the bed of particles, various complicated physical mechanisms are at play that can affect the behavior of the drag force experienced by the particles. There are three primary mechanisms. (i) As the transmitted shock travels along the bed of particles, particles diffract the flow field. This diffraction is in the form of compression and rarefaction waves, which radiate away from the spherical particles. These compression waves distort the transmitted shock wave. Figures 12(a) and 12(b) illustrates this phenomenon. As the transmitted shock continues to

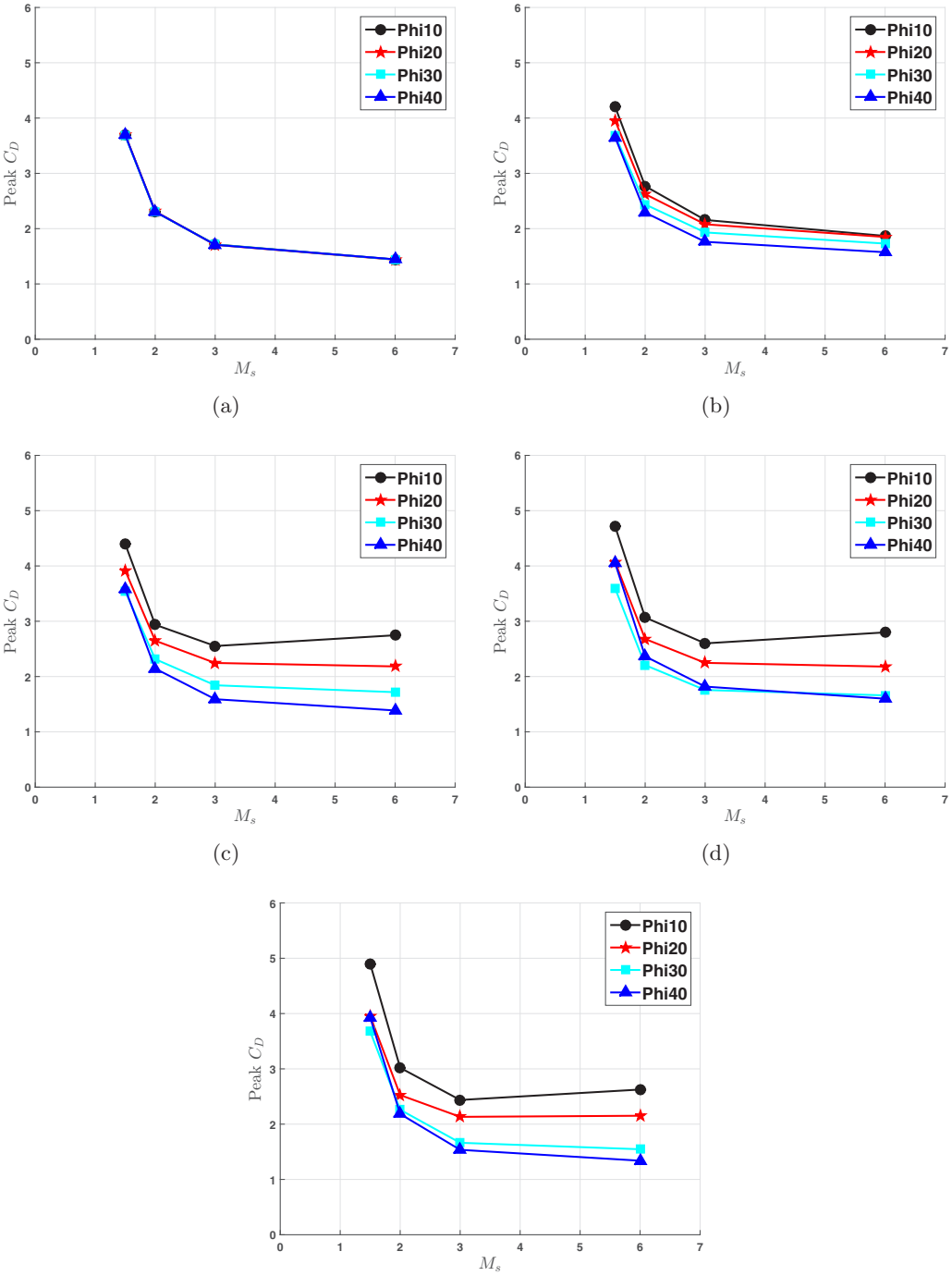

FIG. 11. Plot of the peak drag coefficient C_D as a function of shock Mach number M_s and volume fraction ϕ at (a) plane 1, (b) plane 2, (c) plane 3, (d) plane 4, and (e) plane 5. Here $\phi = 10\%$ (black circles), 20% (red stars), 30% (cyan squares), and 40% (blue triangles).

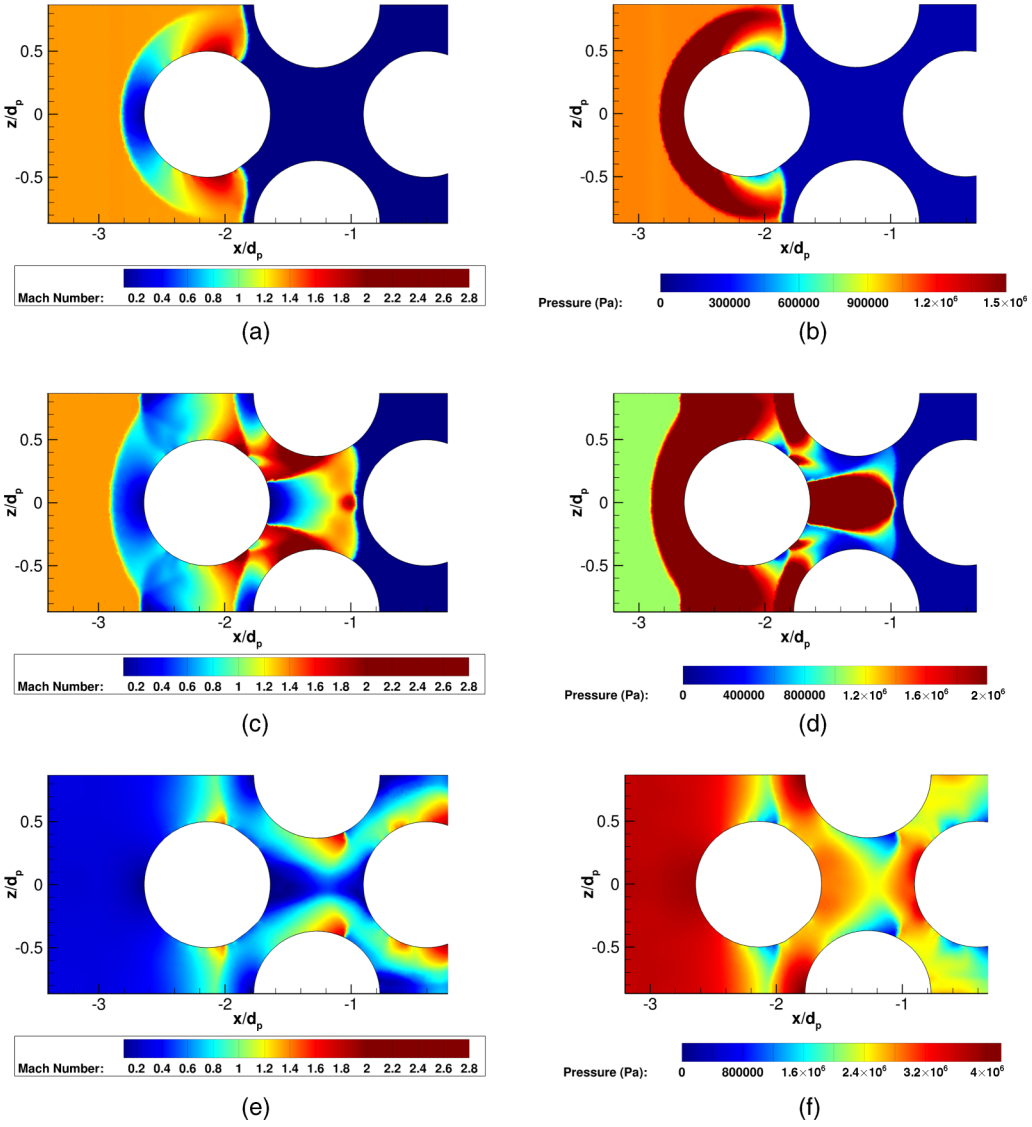

FIG. 12. Contour plots of (a), (c), and (e) Mach number and (b), (d), and (f) pressure for $M_s = 3$ and $\phi = 40\%$ for times (a) and (b) $t/\tau = 1.27$, (c) and (d) $t/\tau = 2.21$, and (e) and (f) $t/\tau = 8.12$. Note that the maximum value of the pressure in the color bar changes.

pass over the particle there is local acceleration of fluid, leading to shock focusing. Figures 12(c) and 12(d) illustrate this phenomenon. Shock focusing results in local pressure amplification and hence a stronger shock is experienced by particles downstream, resulting in an increase in drag force experienced by the downstream particles. (ii) For the shock Mach numbers under consideration in this study, the postshock Mach numbers are greater than or equal to 0.6; recall that 0.6 is the critical Mach number for an isolated sphere, since at this Mach number the flow around an isolated sphere is locally sonic. Because of supercritical flow there is formation of shocklets around the spheres for most of the simulations. Figures 12(e) and 12(f) illustrate this phenomenon. Shocklets dissipate energy from the transmitted shock as it travels along the particle bed. This dissipation of energy results in weakening of the transmitted shock and hence reduction in the drag force. (iii)

As the transmitted shock travels through the bed of particles, the flow field is diffracted because of the presence of the particles. This diffracted flow field around each particle coalesces to form constructive or destructive interference.

The incoming shock diffracts around each plane of particles and coalesces behind the plane of particles as it propagates through the bed of particles. At the volume fractions under consideration, the streamwise distance between the subsequent planes of particles is sufficiently small that the transmitted shock remains nonplanar as it encounters the next plane of particles. As a result, pressure distribution shows large variation across the y-z plane as the transmitted shock passes over it. There are regions of high and low pressure due to constructive and destructive interference of the diffracted flow. The interference pattern depends on parameters such as interparticle spacing (or volume fraction) and incident shock Mach number. Instances where the next plane of particles is subjected to high shock pressure contribute to increased drag, while instances where the next plane of particles is subjected to lower pressure contribute to decreased drag.

All these mechanisms are strongly affected by the volume fraction and the shock Mach number. At any given instant of time, the cumulative effect of all these mechanisms affects the drag experienced by the particles, which results in the various trends observed in Figs. 7–10.

To better understand this behavior, contour plots of the local Mach number along the x-z plane at $y = 0$ are plotted in Figs. 13 and 14. As before, the x and z directions are nondimensionalized by the particle diameter d_p. All the plots are at the nondimensional time $t/\tau \sim 12$. The cases shown in Fig. 13 correspond to the diagonal of Table II (i.e., going from $M_s = 1.5$ and $\phi = 10\%$ to $M_s = 6$ and $\phi = 40\%$), while Fig. 14 corresponds to the third column (i.e., $M_s = 3.0$ and varying ϕ). For Fig. 13(a) ($M_s = 1.5$ and $\phi = 10\%$), we see a reflected rarefaction wave traveling upstream of the particle bed. This shows that for low volume fractions and near subcritical shock Mach numbers, the reflected waves from particles of plane 1 are not strong enough to coalesce to form a shock wave. The flow adjacent to the particles in planes 2–4 is either subsonic or close to sonic, whereas the flow adjacent to the particles in plane 5 is supersonic forming shocklets. This results in a close to zero average drag force on the particles in planes 1–4 and nonzero drag on particles in plane 5 because of the presence of the shocklet.

For Fig. 13(b) ($M_s = 2.0$ and $\phi = 20\%$), the reflected wave from plane 1 propagating upstream is also subsonic. However, with a decrease in particle spacing and an increase in shock Mach number, there are shocklets that form for all the particles in planes 1–4, with a strong supersonic flow attached to the particles in plane 5.

For Figs. 13(c) and 13(d), the reflected wave propagating upstream of plane 1 is now a reflected shock wave. This reflected shock wave does not reach a steady state during the simulation time under consideration. In this sense it differs from the collective bow shock observed in front of particles in a transverse array [24]; the difference can be attributed to the fact that here we have transverse periodicity. Similar to Fig. 13(b), the particles in planes 1–4 have shocklets attached to them, which results in nonzero drag. Note that the particles in plane 5 have a strong shocklet and supersonic flow locally and hence a high nonzero drag at later times, as observed in Figs. 7–10.

To study the effect of volume fraction, we plot contours of the local Mach number in Fig. 14 for $M_s = 3.0$ and different volume fractions. We observe that particles in all the planes have shocklets around them. In addition, the intensity of the shocklets in plane 1 decreases as the volume fraction increases. Furthermore, the reflected shock wave travels faster upstream as the volume fraction increases, which might be due to throttling of the back flow because of closely packed particles. Finally, there is a strong supersonic flow just downstream of the particles in plane 5, consistent with observations for the earlier cases.

3. Pressure attenuation behind the particle array

It is clear from the contour plots of the local Mach number of the previous section that shock interaction with particles leads to a transmitted shock, which travels through the bed and downstream of the particle array, and a reflected wave, which travels upstream of the particle array. In this section

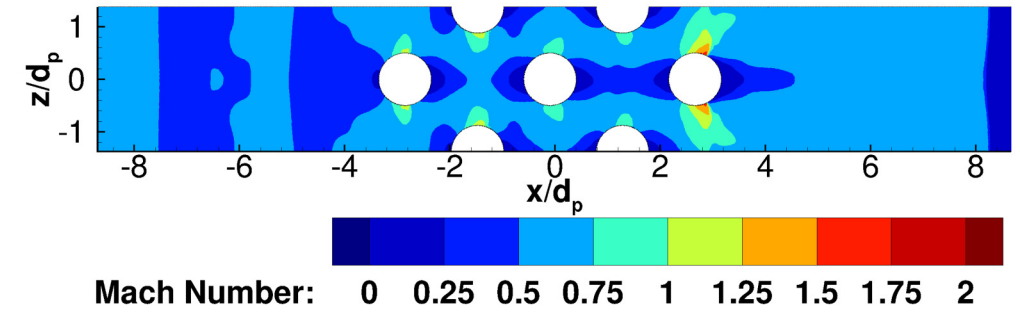

(a)

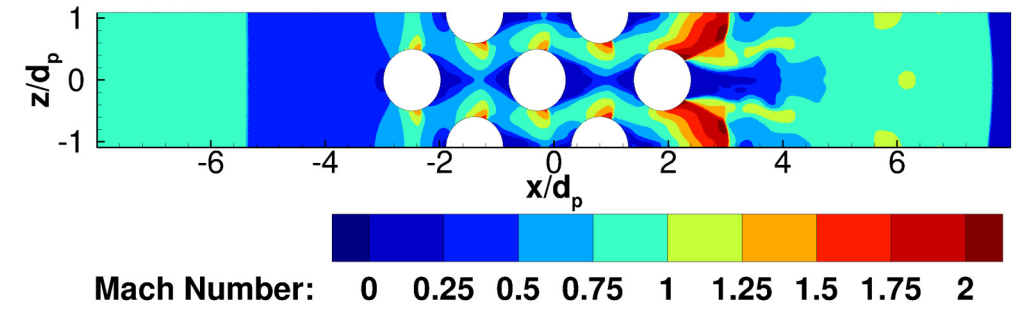

(b)

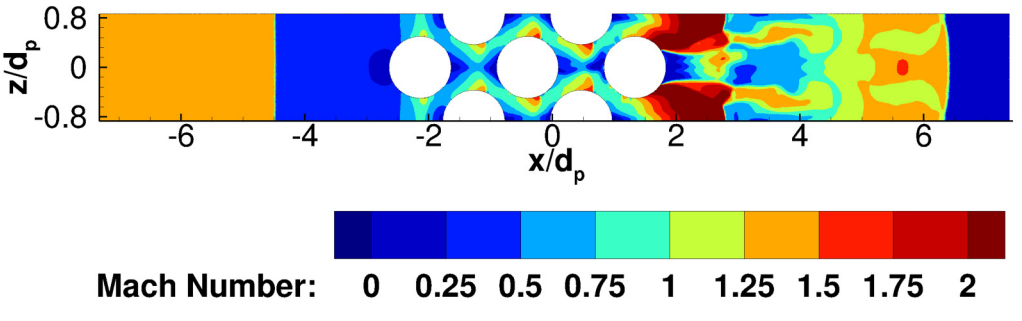

(c)

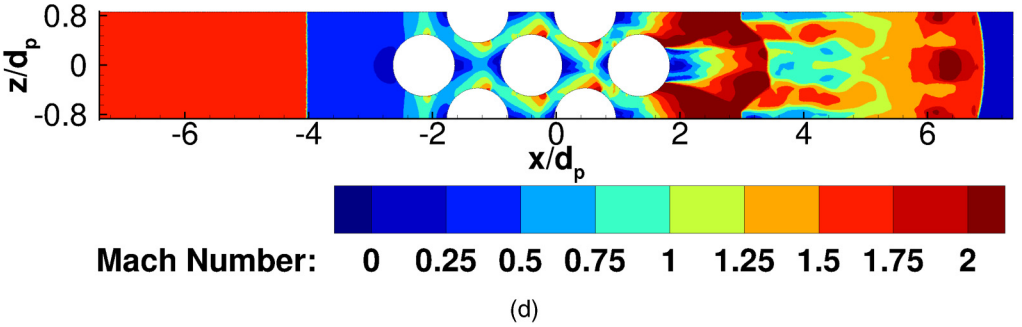

(d)

FIG. 13. Contour plot of Mach number along the x-z plane at $y = 0$ for (a) $\phi = 10\%$ and $M_s = 1.5$, (b) $\phi = 20\%$ and $M_s = 2.0$, (c) $\phi = 30\%$ and $M_s = 3.0$, and (d) $\phi = 40\%$ and $M_s = 6.0$.

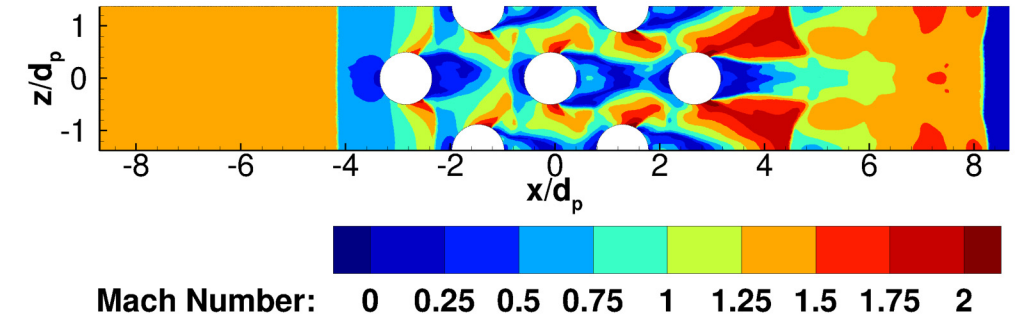

(a)

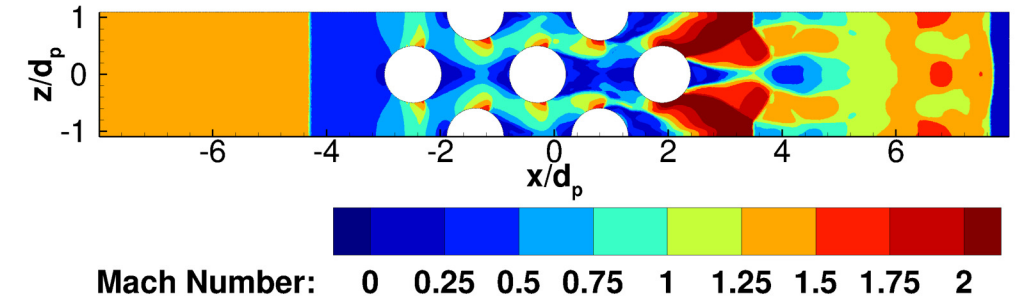

(b)

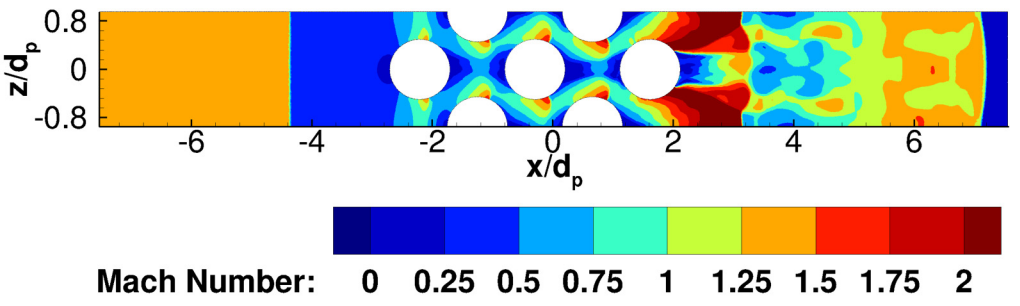

(c)

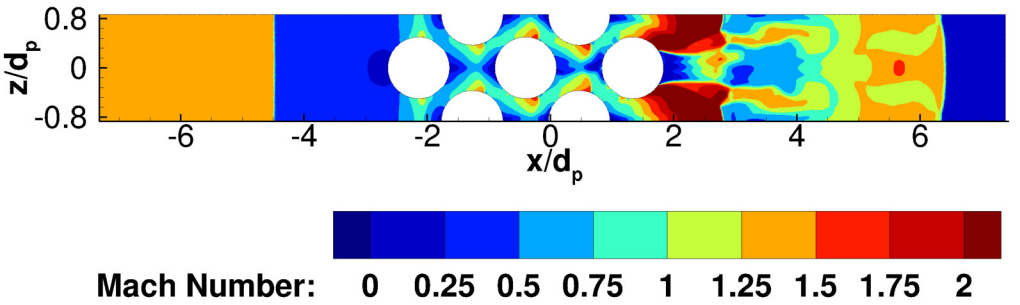

(d)

FIG. 14. Contour plot of Mach number along the x-z plane at $y = 0$ for $M_s = 3.0$ and (a) $\phi = 10\%$, (b) $\phi = 20\%$, (c) $\phi = 30\%$, and (d) $\phi = 40\%$.

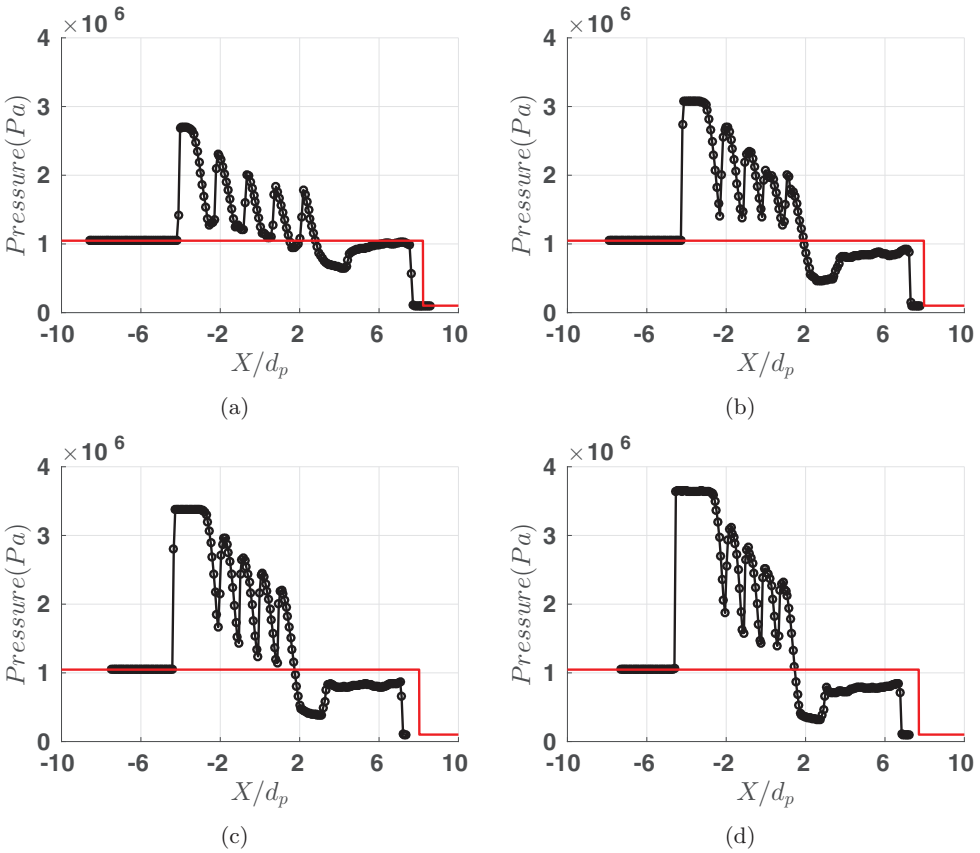

FIG. 15. Plot of plane-averaged pressure along the y-z plane at multiple streamwise locations in the computational domain for $M_s = 3.0$ and (a) $\phi = 10\%$ and $t/\tau = 12.06$, (b) $\phi = 20\%$ and $t/\tau = 11.4$, (c) $\phi = 30\%$ and $t/\tau = 11.2$, and (d) $\phi = 40\%$ and $t/\tau = 10.8$. Here pressure is in the presence of the particles (black curve with circles) and pressure is in the absence of the particles (red curve).

we plot the averaged streamwise pressure in the computational domain to determine the strength of the transmitted shock. This is done to better understand the impact of the particles on the flow and to investigate the pressure attenuation or amplification behind the particle (porous) barrier. Two hundred slices are taken along the y-z planes at equispaced streamwise locations. Note that the slices are more coarse than a typical computational cell size. The plane-averaged pressure is then computed for each slice. Results for $M_s = 3$ and various volume fractions at a fixed time $t/\tau \sim 11$ are presented in Fig. 15; results for the other shock Mach numbers show similar trends and so are not shown here. In the figure we also plot the pressure in the absence of the particles (red), which is given as a comparison in order to highlight the effect of particles on the flow. For each volume fraction, the reflected wave is located at $x/d_p \approx -4$, while the transmitted shock wave is located at $x/d_p \approx 7$. Note that for a given shock Mach number, the pressure loss for the transmitted shock and the strength of the reflected wave increase as the volume fraction increases. Between the reflected and transmitted waves the plane-averaged pressure oscillates. These oscillations are a direct consequence of the flow through the fcc array, where the local pressure can be larger or smaller than the either the postshock pressure or the averaged pressure. Similar results are shown for numerical simulations two-dimensional random packs of disks [22]. This is better visualized in Fig. 16, where the corresponding pressure contours are plotted. In this figure we see that for the volume fraction of $\phi = 10\%$, there is a high-pressure region just upstream of the first plane of

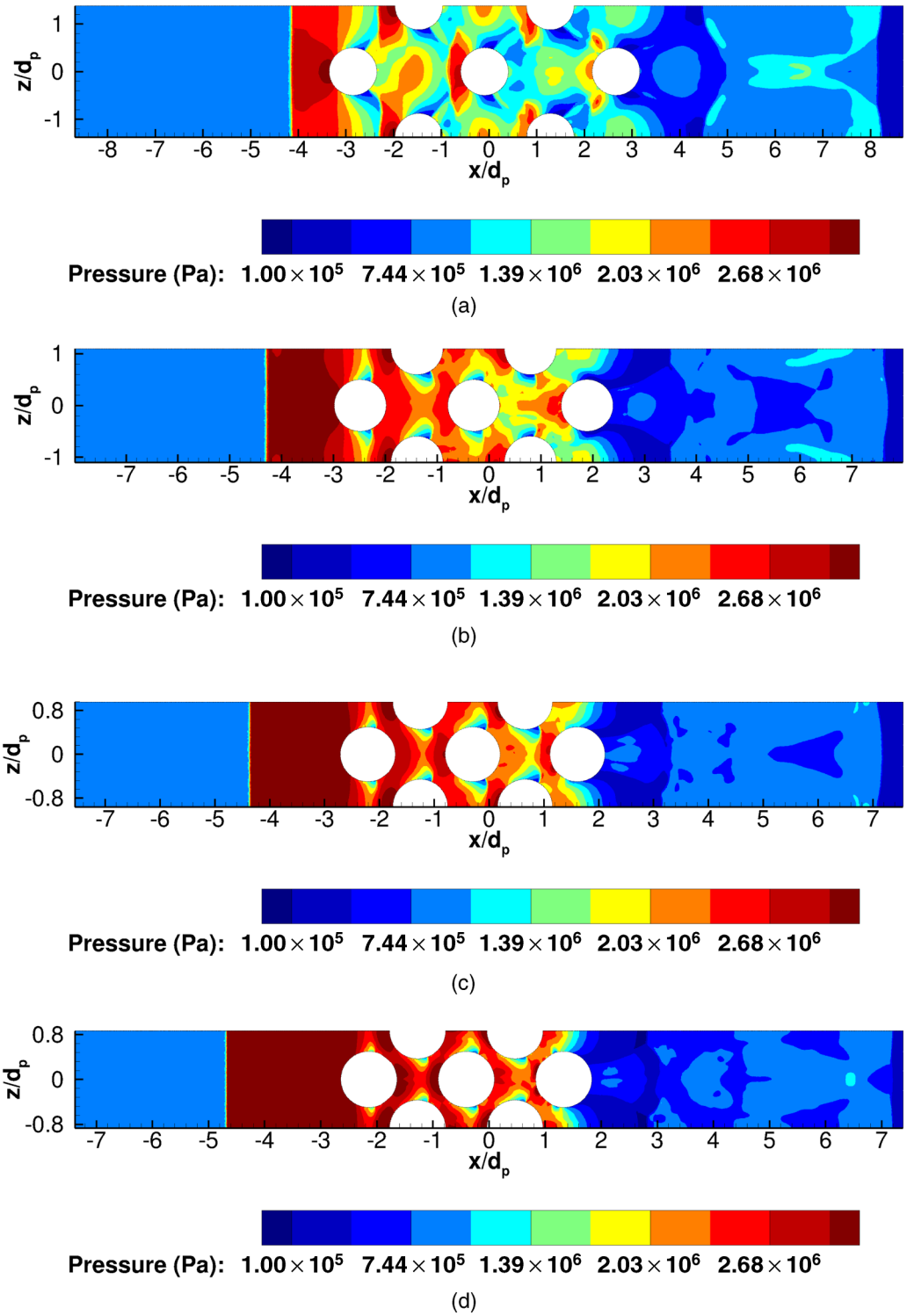

FIG. 16. Contour plot of pressure along the x-z plane at $y = 0$ for $M_s = 3.0$ and (a) $\phi = 10\%$ and $t/\tau = 12.06$, (b) $\phi = 20\%$ and $t/\tau = 11.4$, (c) $\phi = 30\%$ and $t/\tau = 11.2$, and (d) $\phi = 40\%$ and $t/\tau = 10.8$.

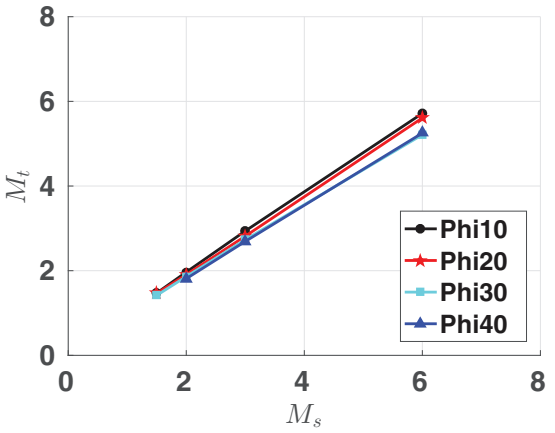

FIG. 17. Plot of the Mach number of the transmitted wave M_t as a function of shock Mach number M_s.

particles. This high-pressure region becomes extended further upstream of the first plane of particles, and reaches deeper into the array, as the volume fraction increases. From the plane-average pressure plots shown in Fig. 15 and for each volume fraction, we see that the transmitted shock travels slower than the corresponding shock wave in the absence of particles; compare the location of the step in the red curve to the location of the transmitted shock. In addition, the plane-average pressure just upstream of the transmitted shock is lower than the corresponding postshock pressure in the absence of particles; again, compare the red curve just upstream of the step with the numerical solutions. Thus, for each volume fraction, we do not observe the pressure amplification reported by Naiman *et al.* [29]. In fact, the pressure downstream of the particle bed is always less than the theoretical pressure (defined as the postshock pressure in the absence of the particles); this is true of all of the other shock Mach numbers (not shown). This suggests that there is a loss in pressure or pressure attenuation for the transmitted shock as it propagates through the fcc array of particles. This averaged pressure loss can be explained by the cumulative effect of physical mechanisms (shocklets and destructive interference of the waves) occurring during shock-particle interaction, as mentioned above and highlighted in Fig. 16. We comment that this observation is only for the averaged pressure; the local pressure can be higher, and this will be discussed below. Note also that for a volume fraction of $\phi = 10\%$, the pressure loss for the transmitted shock wave is negligible; this is true for all shock Mach numbers (results not shown).

Although, as shown in Fig. 15, the pressure behind the transmitted shock averaged over the y-z plane always remains lower than in the absence of the particles, locally there may be regions where the pressure can be higher. For example, for the $M_s = 3.0$ case, if the pressure is higher than 1.047 MPa then the increase in pressure must be due to the shock focusing effect as it passes through the fcc array. In Fig. 16(a) we see a substantial region between $x = 5.0$ and 8 (shaded in cyan) where the pressure exceeds 1.047 MPa. In fact, at the time shown in Fig. 16(a), the peak pressure in the wake reaches a peak value of about 1.4 MPa (40% higher than the postshock pressure without the particle array). With increasing volume fraction, the regions of higher pressure decreases and is virtually absent at a volume fraction of 30% and larger. This is consistent with observations made in the literature that shock propagation through a porous media can increase the pressure downstream. However, this is a localized phenomenon, and when averaged over a larger region the net pressure always attenuates.

Results for all the simulations are summarized in Fig. 17, where the Mach number of the transmitted shock wave M_t is computed. Note that M_t is relatively insensitive to particle volume fraction.

IV. CONCLUSION

An investigation of shock propagation through a face centered cubic array was presented. Three-dimensional numerical simulations were carried out and results varying the volume fraction and primary shock Mach number were given. We found that the drag-time curve over each plane of particles in the fcc array is strongly influenced by the volume fraction and shock Mach number. In particular, at a shock Mach number of 1.5, the late time unsteady drag for particles in the last plane increases as the volume fraction increases, suggesting that the particles in the last plane in the fcc array will tend to move faster than the particles in the upstream planes. On the other hand, for a shock Mach number of 6.0, the late time drags among all of the planes are roughly the same for all volume fractions, suggesting that the particles will tend to move together. We also plotted the peak drag and showed that the effect of increasing the volume fraction is to decrease the drag at a fixed shock Mach number. To better understand particle-particle interactions, we also showed the corresponding contour plots of the local Mach number at a fixed nondimensional time. For most cases, shocklets form around each plane of particles, while the flow just downstream of the last plane of particles is supersonic. As the transmitted shock propagates through the fcc array, the flow field becomes diffracted and this diffracted flow and the reflections that are produced coalesce to form constructive or destructive interference, which results in an increase or decrease in the drag force, respectively. Finally, we showed that there is a weakening of the transmitted shock as it travels through the fcc array since shocklets dissipate energy. This has important consequences in modeling the pressure attenuation behind porous barriers.

The numerical work presented here on shock interaction with a face centered cubic array complements our previous work on shock-particle interaction over simple arrangements [23,24,35]. Taken together, we found that the drag for a single particle is significantly altered when neighboring particles are present. At the macroscale, using standard drag laws for an isolated particle maybe inadequate to properly account for particle-particle interactions when a group of particles are present. Thus, there is a need to better understand and model drag when considering a group of particles for macroscale simulations. To this end, future work should consider three-dimensional simulations of random packs of spheres, where both the volume fraction and primary shock Mach number are varied.

ACKNOWLEDGMENTS

This work was supported in part by the U.S. Department of Energy, National Nuclear Security Administration, Advanced Simulation and Computing Program, as a Cooperative Agreement under the Predictive Science Academic Alliance Program, under Contract No. DE-NA0002378. T.L.J. was also supported in part by the Defense Threat Reduction Agency, Basic Research Award No. HDTRA1-14-1-0031 to University of Florida; S.B. was also supported in part by the Defense Threat Reduction Agency, Basic Research Award No. HDTRA1-14-1-0028 to University of Florida.

[1] A. W. Woods, The fluid dynamics and thermodynamics of eruption columns, Bull. Volcanol. **50**, 169 (1988).

[2] G. Tancredi, J. Ishitsuka, P. H. Schultz, R. S. Harris, P. Brown, D. O. ReVelle, K. Antier, A. LePichon, D. Rosales, E. Vidal, M. E. Varela, L. Sanchez, S. Benavente, J. Bojorquez, D. Cabezas, and A. Dalmau, A meteorite crater on Earth formed on September 15, 2007: The Carancas hypervelocity impact, Meteorit. Planet. Sci. **44**, 1967 (2009).

[3] M. Scholer and G. Morfill, Simulation of solar flare particle interaction with interplanetary shock waves, Sol. Phys. **45**, 227 (1975).

[4] T. Saito, M. Saba, M. Sun, and K. Takayama, The effect of an unsteady drag force on the structure of a non-equilibrium region behind a shock wave in a gas-particle mixture, Shock Waves **17**, 255 (2007).
[5] V. M. Boiko, V. P. Kiselev, S. P. Kiselev, A. N. Papyrin, S. V. Poplavsky, and V. M. Fomin, Shock wave interaction with a cloud of particles, Shock Waves **7**, 275 (1997).
[6] J. Wagner, S. J. Beresh, S. P. Kearney, W. M. Trott, J. N. Castaneda, B. O. Pruett, and M. R. Baer, A multiphase shock tube for shock wave interactions with dense particle fields, Exp. Fluids **52**, 1507 (2012).
[7] J. L. Wagner, S. J. Beresh, S. P. Kearney, B. O. M. Pruett, and E. K. Wright, Shock tube investigation of quasi-steady drag in shock-particle interactions, Phys. Fluids **24**, 123301 (2012).
[8] Y. Ling, J. L. Wagner, S. J. Beresh, S. P. Kearney, and S. Balachandar, Interaction of a planar shock wave with a dense particle curtain: Modeling and experiments, Phys. Fluids **24**, 113301 (2012).
[9] O. Igra and K. Takayama, Shock tube study of the drag coefficient of a sphere in a non-stationary flow, Proc. R. Soc. London **442**, 231 (1993).
[10] A. Britan, T. Elperin, O. Igra, and J. P. Jiang, Acceleration of a sphere behind planar shock waves, Exp. Fluids **20**, 84 (1995).
[11] H. Tanno, K. Itoh, T. Saito, A. Abe, and K. Takayama, Interaction of a shock with sphere suspended in a vertical shock tube, Shock Waves **13**, 191 (2003).
[12] H. Tanno, T. Komuro, M. Takahashi, K. Takayama, H. Ojima, and S. Onaya, Unsteady force measurement technique in shock tubes, Rev. Sci. Instrum. **75**, 532 (2004).
[13] M. Sun, T. Saito, K. Takayama, and H. Tanno, Unsteady drag on a sphere by shockwave loading, Shock Waves **14**, 3 (2005).
[14] E. Loth, Compressibility and rarefaction effects on drag of a spherical particle, AIAA J. **46**, 2219 (2008).
[15] M. Parmar, A. Haselbacher, and S. Balachandar, Modeling of the unsteady force for shock-particle interaction, Shock Waves **19**, 317 (2009).
[16] M. Parmar, A. Haselbacher, and S. Balachandar, Equation of motion for a sphere in non-uniform compressible flow, J. Fluid Mech. **699**, 352 (2010).
[17] M. Parmar, A. Haselbacher, and S. Balachandar, Generalized Basset-Boussinesq-Oseen Equation for Unsteady Forces on a Sphere in a Compressible Flow, Phys. Rev. Lett. **106**, 084501 (2011).
[18] A. V. Fedorov, A. V. Shul'gin, and S. V. Poplavski, Motion of a particle behind the shock wave front, Combust. Explo. Shock Waves **46**, 207 (2005).
[19] Y. Ling, A. Haselbacher, and S. Balachandar, Importance of unsteady contributions to force and heating for particles in compressible flow, Part 1: Modeling and analysis for shock-particle interaction, Int. J. Multiphase Flow **37**, 1026 (2011).
[20] Y. Ling, A. Haselbacher, S. Balachandar, F. M. Najjar, and D. S. Stewart, Shock interaction with a deformable particle: Direct numerical simulation and point-particle modeling, J. Appl. Phys. **113**, 013504 (2013).
[21] C. Lu, S. Sambasivan, A. Kapahi, and H. S. Udaykumar, Multi-scale modeling of shock interaction with a cloud of particles using an artificial neural network for model representation, Proc. IUTAM **3**, 25 (2012).
[22] J. D. Regele, J. Rabinovitch, T. Colonius, and G. Blanquart, Unsteady effects in dense, high speed, particle laden flows, Int. J. Multiphase Flow **61**, 1 (2014).
[23] P. Sridharan, T. L. Jackson, J. Zhang, and S. Balachandar, Shock interaction with one-dimensional array of particles in air, J. Appl. Phys. **117**, 075902 (2015).
[24] Y. Mehta, T. L. Jackson, J. Zhang, and S. Balachandar, Numerical investigation of shock interacting with one-dimensional transverse array of particles in air, J. Appl. Phys. **119**, 104901 (2016).
[25] K. Suzuki, H. Himeki, T. Watanuki, and T. Abe, Experimental studies on characteristics of shock wave propagation through cylinder array, Inst. Space Astronaut. Sci. **676**, 1 (2000).
[26] A. Chaudhuri, A. Hadjadj, O. Sadot, and G. Ben-Dor, Numerical study of shock-wave mitigation through matrices of solid obstacles, Shock Waves **23**, 91 (2013).
[27] B. Rogg, D. Hermann, and G. Adomeit, Shock-induced flow in regular arrays of cylinders and packed beds, Int. J. Heat Mass Transfer **28**, 2285 (1985).
[28] D. B. Epstein and A. N. Kudryavtsev, in *28th International Symposium on Shock Waves*, edited by K. Kontis (Springer, Berlin, 2012), Vol. 2, pp. 537–542.

[29] H. Naiman and D. D. Knight, The effect of porosity on shock interaction with a rigid, porous barrier, Shock Waves **16**, 321 (2007).
[30] M.-S. Liou, A Sequel to AUSM: AUSM$^+$, J. Comput. Phys. **129**, 364 (1996).
[31] A. Haselbacher, *Proceedings of the AIAA Aerospace Sciences Meeting and Exhibit* (AIAA, Reston, 2005), paper 2005-0879.
[32] A. Haselbacher, S. Balachandar, and S. W. Kieffer, Open-ended shock-tube flows: Influence of pressure ratio and diaphragm position, AIAA J. **45**, 1917 (2007).
[33] P. R. Eiseman, GRIDPRO v6.1, *Topology Input Language Manual* (Program Development Company, White Plains, 2016).
[34] H. Si, TetGen, A Delaunay-based quality tetrahedral mesh generator, ACM Trans. Math. Softw. **41**, 11 (2015).
[35] P. Sridharan, T. L. Jackson, J. Zhang, S. Balachandar, and S. Thakur, Shock interaction with deformable particles using a constrained interface reinitialization scheme, J. Appl. Phys. **119**, 064904 (2016).
[36] F. S. Billing, Shock-wave shapes around spherical- and cylindrical-nosed bodies, AIAA J. Spacecraft **4**, 822 (1967).
[37] S. F. Hoerner, *Fluid-Dynamic Drag* (Hoerner, Midland Park, 1965).
[38] C. T. Crowe, W. R. Babcock, and P. G. Willoughby, Drag coefficient for particles in rarefied, low Mach-number flows, Prog. Heat Mass Transfer **6**, 419 (1972).